

Kinks in the electronic dispersion of the Hubbard model away from half filling

Patrick Grete, Sebastian Schmitt, Carsten Raas, Frithjof B. Anders, and Götz S. Uhrig
*Technische Universität Dortmund, 44221 Dortmund, Germany**

(Dated: October 26, 2018)

We study kinks in the electronic dispersion of a generic strongly correlated system by dynamic mean-field theory (DMFT). The focus is on doped systems away from particle-hole symmetry where valence fluctuations matter potentially. Three different algorithms are compared to assess their strengths and weaknesses as well as to clearly distinguish physical features from algorithmic artefacts. Our findings extend a view previously established for half-filled systems where kinks reflect the coupling of the fermionic quasiparticles to emergent collective modes, which are identified here as spin fluctuations. Kinks are observed when strong spin fluctuations are present and, additionally, a separation of energy scales for spin and charge excitations exists. Both criteria are met by strongly correlated systems close to a Mott-insulator transition. The energies of the kinks and their doping dependence fit well to the kinks in the cuprates, which is surprising in view of the spatial correlations neglected by DMFT.

PACS numbers: 71.27.+a, 71.30.+h, 74.25.Jb, 71.28.+d

I. INTRODUCTION

Collective bosonic modes can modify the low-energy electronic properties on the characteristic energy scale of these bosonic excitations. Well understood are the significant mass enhancement¹ and the kinks in the electronic dispersion² in materials with strong electron-phonon coupling. These kinks are abrupt changes of the slope of the electronic dispersion which occur at energies of the order of the Debye energy which is much smaller than the Fermi energy in such systems.

In this paper we study kinks in the electronic dispersion which are related to emergent collective bosonic modes of the purely electronic system rather than by a coupling to external bosons such as phonons. It was shown by Byczuk et al. in the framework of dynamic mean-field theory^{3,4} (DMFT) that such kinks are a generic feature of strongly interacting systems and require no externally coupled bosons.⁵ Their argument resides on the structure of the DMFT equations and the spectral density of the local propagator.

Our work supplements the mathematical argument in Ref. 5 by the physical picture that the *internally generated* emergent collective modes provide the bosons which generate the kinks in the dispersion. This point of view has been already put forward for the half-filled case where the physical situation is particularly clear.⁶ We will show that in the model studied below these collective modes are spin fluctuations of local moments formed due to the strong local Coulomb interaction. In the Mott insulating phase, stable local moments are generated which tend to form magnetically ordered phases due to residual spin-spin interactions. In the metallic phase, however, these local moments are completely screened at zero energy and the spin fluctuations at intermediate energies live only for a finite time because they decay into particle-hole pairs (Landau damping). We call the spin fluctuations appearing as resonances emergent modes because they become long-lived for even larger interaction in the insulating

phase. Photoemission experiments support our view in antiferromagnetic^{7–9} and in ferromagnetic systems.¹⁰

As will be shown, there exist two conditions for the kinks to appear in the dispersion relation. For one, strong emergent collective modes (spin fluctuations) must be present in the system. This is signaled by a pronounced maximum in the imaginary part of the spin susceptibility at a finite energy ω_{\max} . For another, the energy scale for charge excitations ω_{charge} must be much larger than the characteristic spin-excitation energy, i.e. $|\omega_{\text{charge}}| \gg |\omega_{\max}|$. Here, the energy scale for charge excitations is set either by a single-particle energy or the characteristic scale for collective charge excitations, depending on which is smaller. Both criteria are met in strongly correlated metallic systems close to a Mott-insulator transition.

The term “collective bosonic modes” in solid-state systems usually refers to dispersive, i.e., wave-vector dependent, excitations such as (para-)magnons or charge density waves. Such modes are characterized by the momentum dependent spin- and charge-susceptibilities $\chi_{\text{mag}}(\vec{q}, \omega)$ and $\chi_{\text{charge}}(\vec{q}, \omega)$, respectively. It may be put forward that in DMFT no true collective modes exist because they do not propagate properly. Indeed, in the strict limit of infinite dimensions collective two-particle properties are local because they are momentum-independent except for some momenta of measure zero.^{11–14} Yet we do not adopt this puristic view and stick to the wording of collective bosonic modes for three reasons. First, spin- and charge fluctuations are two-particle properties and as such comprise at least two elementary fermionic excitations so that they are collective and bosonic in this sense. Second, even in the strict DMFT, the spin- and charge-susceptibilities are true lattice quantities involving all lattice sites. Otherwise, their imaginary parts would show only one or two δ peaks instead of broad continua, see for instance Ref. 15. Third, generically the DMFT is taken as an approximation to finite dimensional systems. Then, the susceptibilities ac-

quire a non-trivial \vec{q} -dependence through the inner momentum and frequency sums in the Bethe-Salpeter equations, even though the irreducible two-particle vertex is assumed to be local.^{16,17} In the present work, we extract the characteristic energy scales relevant for the dispersive collective modes from the local susceptibilities $\chi(\omega) = \frac{1}{N} \sum_{\vec{q}} \chi(\vec{q}, \omega)$ because they readily reflect these energy scales and can be obtained in DMFT from the effective impurity model.

We investigate the low-temperature phase of the Hubbard model away from half filling using the DMFT with three different impurity solvers in order to be able to clearly separate physical features from possible algorithmic artifacts. We employ two numerical renormalization schemes, namely the density-matrix renormalization group¹⁸ (DMRG) and numerical renormalization group¹⁹ (NRG) as well as a diagrammatic approach, the so-called enhanced non-crossing approximation (ENCA).^{20,21} The results of all three algorithms agree very well. The remaining differences can be understood on the basis of the known strengths and weaknesses of the approaches.

The prevailing effect of the interaction is a significant renormalization of the bare electron mass due to correlations. The Fermi liquid theory²² connects this mass renormalization to a fundamental energy scale T^* below which the Fermi liquid picture of renormalized weakly interacting, long-lived quasiparticles applies. In strongly correlated electron systems the properties of these renormalized quasiparticles may differ dramatically from those of non-interacting electrons as exemplified in heavy fermion systems.^{23,24}

The article is laid out as follows. The model and the relevant theoretical background are described Sec. II. In particular, the basic ideas of all three impurity solvers are discussed. In order to gauge their differences a comparison of the single-particle dynamics is shown in Sec. III. We begin with the results for the self-energies. Then we turn to the extraction of the Fermi liquid low energy scale T^* and relate it to the maxima in the local charge and spin susceptibilities. in Sec. IIIB. We will explicitly show that T^* also occurs as energy scale in the dynamic spin susceptibility but not in the local charge susceptibility. Therefore, the connection made between emergent spin-fluctuations and the kinks in the electronic dispersion⁶ extends to the metallic regime away from half filling. This main results of our work is contained in Sec. IV where also the doping dependence of the kink energies is compared to experimental results. Finally, our findings are summarized in Sect. V.

II. MODEL AND METHODS

A. Hubbard Model and Dynamic Mean-Field Theory

We consider the single-band Hubbard model which is the simplest model for correlated electrons on a lattice

$$\mathcal{H} = -t \sum_{\langle i,j \rangle, \sigma} (c_{i\sigma}^\dagger c_{j\sigma} + c_{j\sigma}^\dagger c_{i\sigma}) + U \sum_i n_{i\uparrow} n_{i\downarrow} - \left(\frac{U}{2} + \mu \right) \sum_{i\sigma} n_{i\sigma}. \quad (1)$$

The operators $c_{i\sigma}^\dagger$ ($c_{i\sigma}$) create (annihilate) electrons with spin $\sigma = \{\uparrow, \downarrow\}$ at lattice sites i and $n_{i\sigma} = c_{i\sigma}^\dagger c_{i\sigma}$ is the occupation number operator. The first term in the Hamiltonian (1) describes electronic hopping with amplitude t , where $\langle i, j \rangle$ indicates nearest neighbor sites. The local Coulomb repulsion is incorporated in the second term with matrix element U . The last term sets the local single-particle levels and includes the chemical potential in a way, that $\mu = 0$ corresponds to an electron-hole symmetric situation, i.e., half-filling.

Despite its simplicity, the exact solution of the Hubbard Hamiltonian (1) has only been possible in one spatial dimension,^{25,26} for a recent book on this topic see Ref. 27. In order to obtain an approximate solution for higher dimensional systems we employ the dynamic mean-field theory (DMFT),^{3,4} for recent reviews see Refs. 28,29.

A non-trivial, but considerable, simplification is obtained in the limit of infinite coordination number (infinite spatial dimension) if the hopping matrix elements are rescaled appropriately.³⁰⁻³² In this limit DMFT represents the exact solution.^{3,4} When applied in finite dimensions, the major approximation of DMFT consists in treating all non-local correlations in a mean-field manner while the correlated local dynamics is faithfully retained. This translates to the self-energy being momentum independent,³¹ $\Sigma(\vec{k}, z) \xrightarrow{\text{DMFT}} \Sigma(z)$ where we use z as a general complex energy argument with finite imaginary part.

Then, the local Green function of the lattice problem reads

$$G(z) = \frac{1}{N} \sum_{\vec{k}} \frac{1}{z + \mu + \frac{U}{2} - \epsilon_{\vec{k}} - \Sigma(z)} \quad (2)$$

where N is the number of lattice sites and $\epsilon_{\vec{k}}$ the bare dispersion. This local lattice propagator equals the local Green function of an effective single-impurity Anderson model (SIAM)

$$G(z) = \frac{1}{z + \mu + \frac{U}{2} - \Gamma(z) - \Sigma(z)} \quad (3)$$

embedded in a medium characterized by the hybridization function $\Gamma(z)$. Thus, the embedding medium is a

dynamic medium and it is not independent from the solution of the SIAM, but it has to be determined self-consistently as in any generic mean-field approach.

For a given guess for the hybridization function the local Green function is determined by a suitable numerical algorithm which is commonly referred to as the employed ‘impurity solver’. This yields the self-energy

$$\Sigma(z) = z + \mu + \frac{U}{2} - \Gamma(z) - G(z)^{-1} \quad , \quad (4)$$

which in turn is used to obtain the local lattice propagator $G(z)$ via Eq. (2). It is in this step that the lattice structure enters. The self-consistency cycle is closed by reorganizing Eq. (4) and to extract a new guess for $\Gamma(z)$. This cycle is iterated until convergence is reached in the pragmatic sense of a tolerable deviation of two successive results for the local Green function, the self-energy, or the hybridization function.

The nontrivial step in this cycle is the solution of the effective SIAM. Due to the long history of DMFT, a multitude of different impurity solvers for treating this model exists such as iterative perturbation theory,^{32–34} exact diagonalization^{35,36} or several variations of quantum Monte-Carlo schemes.^{16,37–40} In this work, we employ the enhanced non-crossing approximation, the numerical renormalization group, and the dynamic density-matrix renormalization group as impurity solvers and compare their results.

B. Enhanced non-crossing approximation

The enhanced non-crossing approximation (ENCA),^{20,21,41,42} sometimes also called one-crossing approximation,⁴³ is a thermodynamically conserving^{44,45} approximation for the SIAM which utilizes the expansion with respect to the hybridization between the impurity electrons and the conduction band.^{46–49} It extends the usual non-crossing approximation (NCA)^{50,51} to finite values of the Coulomb repulsion U via the incorporation of the lowest order vertex corrections, which are necessary to produce the correct Schrieffer-Wolff exchange coupling and the order of magnitude of the low energy Kondo scale T_K in the problem. The impurity spectral function²⁰ and dynamic susceptibilities⁵² are extracted directly for real frequencies without any adjustable parameters.

The NCA is known to violate Fermi liquid properties at very low temperatures and some pathological structure appears at the Fermi level below a pathology scale.^{53,54} The ENCA removes the cusps associated with this pathology²⁰ and significantly improves the Fermi liquid properties of the spectral functions and dynamic susceptibilities.^{17,52} However, the skeleton diagrams selected within the ENCA still suffer from an imbalance between charge and spin excitations. While magnetic properties, i.e., the magnetic susceptibility, are described excellently, charge fluctuations are not as well accounted

for.⁵² In the spectral functions, where spin and charge fluctuations contribute equally, this leads to an overestimation of the height of the many-body resonance at the Fermi level at too low temperatures. The dynamic charge susceptibility is overestimated for very low frequencies. These shortcomings are related to the threshold exponents of the auxiliary ionic propagators and tend to be worse in parameter regimes with substantial valence fluctuations, i.e., in the mixed valence regime or at small Coulomb repulsions U .

Within the DMFT the overestimation of the many-body resonance of the impurity solution might lead to a violation of causality in the self-energy due to the subtraction occurring in Eq. (4). In parameter regimes with considerable valence fluctuations, i.e., at small U or at large doping, this fact limits DMFT calculations to temperatures above the characteristic low temperature scale T^* of the lattice. Because $T^* \rightarrow 0$ on approaching the Mott-Hubbard metal-to-insulator transition (MIT) the ENCA can be used as impurity solver down to very low temperatures in the vicinity of the MIT.

Detailed comparisons of various approximations based on the hybridization expansion can be found in the literature, e.g., in Refs. 3, 41, 55, and 56.

C. Numerical renormalization group

The NRG is a very powerful tool for accurately calculating equilibrium properties of complex quantum impurities. Originally developed for treating the single-channel Kondo Hamiltonian,⁵⁷ this non-perturbative approach was successfully extended to the Anderson impurity model^{58,59} and other more complex quantum impurities.¹⁹ At the heart of this approach is a logarithmic discretization of the continuous conduction band, controlled by the discretization parameter⁵⁷ $\Lambda > 1$. Using an appropriate unitary transformation, the discretized Hamiltonian is mapped onto a semi-infinite chain, with the impurity coupled to the open end. The N th link along the chain represents an exponentially decreasing energy scale, $\omega_N \propto \Lambda^{-N/2}$. Using this hierarchy of scales, the sequence of finite-size Hamiltonians \mathcal{H}_N for the N -site chain is solved iteratively, discarding the high-energy states at the end of each step to maintain a manageable number of states. The reduced basis set of \mathcal{H}_N thus obtained is expected to faithfully describe the spectrum of the full Hamiltonian on a scale of ω_N , corresponding to the temperature $T_N \sim \omega_N$.⁵⁷ Because the thermal Boltzmann factors suppress the contributions of higher lying energy states exponentially, the reduced NRG basis set of \mathcal{H}_N is sufficient for an accurate calculation of thermodynamic quantities at temperature T_N .

Dynamical quantities, however, such as impurity Green functions and susceptibilities, require the information on all energy scales. In a recent extension of the NRG to real-time dynamics out of equilibrium^{60,61} a com-

plete basis set for a Wilson chain of length N has been identified which is also used for the accurate calculation of spectral functions.^{62,63} Additionally, the discretization error is reduced by averaging over several different discretizations of the conduction band.⁶⁴ In order to reduce the arbitrariness in the spectral broadening^{65–67} the single-particle self-energy entering the DMFT equations is obtained from an exact expression of a ratio of two correlations functions.⁶⁵ Since the local dynamic bosonic spin and charge susceptibilities are calculated directly from the NRG raw data⁶² more pronounced broadening artifacts occur.

In this work we use a discretization parameter $\Lambda = 2$ and keep approximately 1700 states in each NRG iteration step. Eight different band discretizations⁶⁴ are averaged and the artificial logarithmic broadening⁶⁵ varies between $b = 0.08$ and $b = 0.2$.

D. Dynamic density matrix renormalization

The DMRG introduced by White^{68,69} in 1992 is an excellent numerical method for one-dimensional quantum systems with open boundary conditions^{18,70} such as the SIAM in linear chain representation. The dimension of the Hamilton matrix grows exponentially with system size. The DMRG provides a well controlled procedure to cut off this growth by selecting an optimum basis set for the desired states, e.g., the ground state or another target state. The optimum basis states are selected from the eigenvectors of a reduced density matrix from which only the largest eigenvalues are retained.

We calculate dynamic quantities at zero temperature such as the advanced Green functions $G(\omega - i\eta) = G^>(\omega - i\eta) + G^<(\omega - i\eta)$ and $G(\omega) = \lim_{\eta \rightarrow 0+} G(\omega - i\eta)$ using

$$G^{\gtrless}(\omega - i\eta) := \left\langle 0 \left| \mathcal{A} \frac{1}{\omega - i\eta \mp \Delta\mathcal{H}} \mathcal{A}^\dagger \right| 0 \right\rangle, \quad (5)$$

where $\Delta\mathcal{H} := \mathcal{H} - E_0$. The imaginary part of $G^{\gtrless}(\omega - i\eta)$ provides the spectral densities which we are aiming at. Several variants of numerical methods were introduced to obtain dynamic quantities, for instance the Lanczos method⁷¹ and the correction vector method.^{72–74} Since the Lanczos method has a limited numerical resolution,^{71,75–77} for details see the analysis in Ref. 78, we use the correction vector method which targets the ground state $|0\rangle$, the excited state $|\mathcal{A}\rangle := \mathcal{A}^\dagger |0\rangle$, and the resolvent applied to the excited state. This additional targeted state $|\xi_\pm\rangle$ is called the correction vector

$$|\xi_\pm\rangle := \frac{1}{\omega - i\eta \pm \Delta\mathcal{H}} |\mathcal{A}\rangle. \quad (6)$$

Technically, one targets both the real and the imaginary part of $|\xi_\pm\rangle$. The Green function $G^<(\omega - i\eta)$ is obtained from the scalar product

$$G^<(\omega - i\eta) = \langle \mathcal{A} | \xi_\pm \rangle \quad (7)$$

for discrete complex frequencies $\omega_j - i\eta_j$, $\eta_j > 0$. In order to obtain $G(\omega)$ at the real axis with continuous spectral density $\rho(\omega) := \text{Im}G(\omega)/\pi$, we use the least-bias deconvolution algorithm.⁷⁹

The key advantage of the correction vector DMRG is a good energy resolution for low *and* high frequencies ω . With correction vector DMRG combined with least-bias deconvolution, local Green functions^{80,81} and local susceptibilities¹⁵ have been computed successfully.

In this work, we use a fixed distance $\Delta\omega = 0.1D$ between two successive frequencies ω_j and ω_{j+1} , the artificial broadening is $\eta_j = 0.1D$. The energy scale D is half the bandwidth. We keep 256 states in the reduced density matrix.

III. COMPARISON OF METHODS

In this section, we present results for the Hubbard model within DMFT using the three impurity solvers introduced in the previous section. The non-interacting density of states (DOS) is given by the semi-ellipse $\rho_0(\omega) = (2/(D\pi))\sqrt{1 - (\omega/D)^2}$.

The NRG and DMRG calculations were done at zero temperature while the ENCA requires a small finite T as discussed in Sect. II B; the used values are given for each result below. The spectral density $\rho(\omega)$ of the Green function is given by $\rho(\omega) = \text{Im}G(\omega)/\pi$ and we similarly define $\Sigma(\omega) := \lim_{\eta \rightarrow 0+} \Sigma(\omega - i\eta)$.

A. Single Particle Dynamics

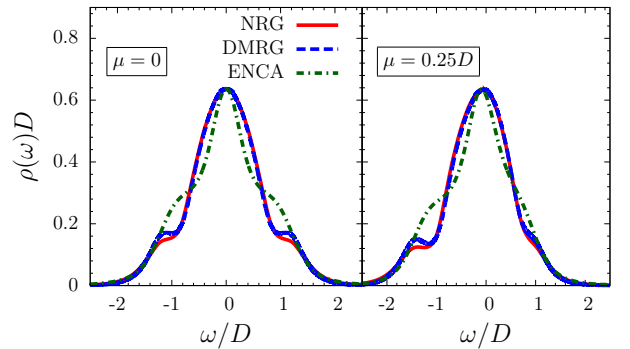


FIG. 1: (Color online) Spectral function for $U = D$ and $\mu = 0$ (left panel) and $\mu = 0.25D$ (right panel). While the NRG and DMRG results are for $T = 0$, the ENCA curves are computed for $T = 0.17D$ (left panel) and for $T = 0.22D$ (right panel). The case $\mu = 0$ implies half-filling, $n = 0.5$, while for $\mu = 0.25D$ the fillings are $n_{\text{NRG}} \approx 0.583$, $n_{\text{DMRG}} \approx 0.577$, and $n_{\text{ENCA}} = 0.573$.

Figure 1 displays a comparison of the local spectral densities for a moderate interaction $U = D$ and for two different values of the chemical potential. All three

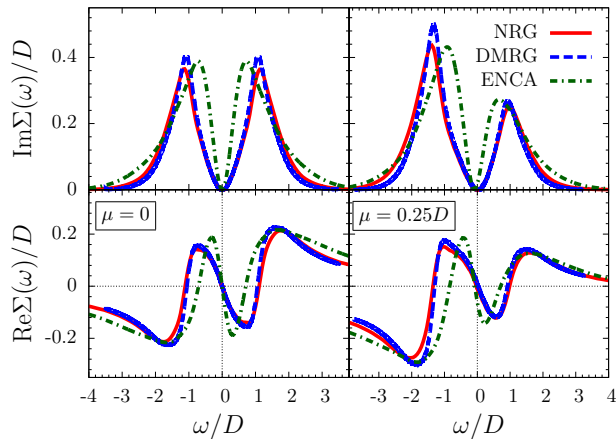


FIG. 2: (Color online) Imaginary (top row) and real (bottom row) parts of the self-energy for $\mu = 0$ (left column) and $\mu = 0.25D$ (right column) and $U = D$. Other parameters are as in Fig. 1

methods qualitatively yield the same result with a broad central peak and only very small shoulders at energies $|\omega| \approx D$. The latter are precursors of the Hubbard bands centered at the energies $\omega \approx \pm U/2 - \mu$. The NRG and DMRG results agree quantitatively and only the shoulders are slightly more pronounced in the DMRG curve which is probably due to the lower resolution of the NRG at high energies. The central resonance of the ENCA curve is narrower and the shoulders of the Hubbard bands are more washed out. The latter feature can be attributed to the rather high temperature, $T \approx 0.17D$ for $\mu = 0$ and $T \approx 0.23D$ for $\mu = 0.25D$, required to avoid the ENCA problems at too low temperatures, see Sect. II.B. At large energies, e.g., $|\omega + \mu| \gtrsim 1.5D$, the spectra of all three methods agree almost perfectly.

The corresponding self-energies are shown in Fig. 2. For all methods the imaginary part $\text{Im}\Sigma(\omega)$ displays a quadratic minimum at the Fermi level signalling the validity of a low-energy effective Fermi liquid description. This implies that the central peak in the spectral function of Fig. 1 is essentially due to Fermi liquid quasiparticle excitations. In accord with the Kramers-Kronig (KK) relation, $\text{Re}\Sigma(\omega)$ behaves linearly at the Fermi level. The self-energies of the renormalization group (RG) approaches NRG and DMRG agree quantitatively and the visible deviations are only due to the different broadening procedures used to obtain continuous functions in ω . The ENCA approach yields a too steep quadratic and linear dependence around the Fermi level in the imaginary and real part, respectively.

B. Collective Modes and Low Energy Scale

The imaginary part of the local dynamic magnetic and charge susceptibilities shown in Fig. 3 shed light on the

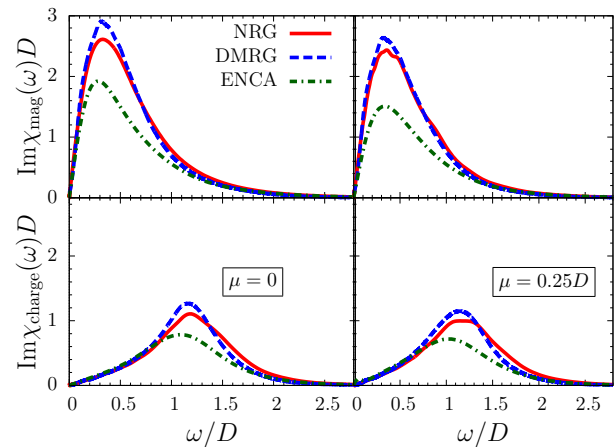


FIG. 3: (Color online) Imaginary part of the magnetic (top row) and charge (bottom row) susceptibility for $\mu = 0$ (left column) and $\mu = 0.25D$ (right column) and $U = D$. Other parameters are as in Fig. 1.

characteristic energies for both types of collective excitations. The characteristic energy for local charge excitations is given by the position of the Hubbard bands as can be observed in Fig. 1. Consequently $\text{Im}\chi_{\text{charge}}(\omega)$ has a broad peak at roughly $\omega \approx 1.1D$. Away from half-filling, the asymmetric position of the lower and the upper Hubbard band is reflected by a slightly broadened peak. Compared to the charge excitations, the characteristic energy for local spin excitations is shifted towards lower values and the absolute height of $\text{Im}\chi_{\text{mag}}(\omega)$ is roughly twice as large as $\text{Im}\chi_{\text{charge}}(\omega)$. Both these features are signs of the enhanced magnetic Kondo-like correlations in the system already present for this moderate value of $U = D$. The overall height of the ENCA susceptibilities is lower than those of the RG approaches due to the nonzero temperature. Additionally, the maxima in the ENCA results are shifted to slightly lower energies.

Increasing the Coulomb repulsion to $U = 2D$ strongly enhances the correlations in the system. At half-filling, this increase drives the system towards the MIT. In the spectral densities depicted in Fig. 4 for half-filling ($\mu = 0$) and for finite chemical potential ($\mu = 0.5D$), the Hubbard bands are now well separated from the many-body resonance at the Fermi level. The inner edges of the Hubbard bands are rather sharp with slight peaks associated presumably with bound trions of a quasiparticle and a particle-hole pair.^{80,81} In the ENCA spectra, such peaks have also been obtained,⁸² but they are not observed here due to the relatively high temperature. The spectra obtained by DMRG and by ENCA are almost indistinguishable at high energies, e.g., for $|\omega + \mu| \gtrsim 1.5D$. The NRG curve falls off slower for large energies due to the limited resolution at large energies mentioned previously.

The deviation between the ENCA and the RG results are partly due to the finite temperature to be used in the ENCA evaluation. Another part is due to a too low

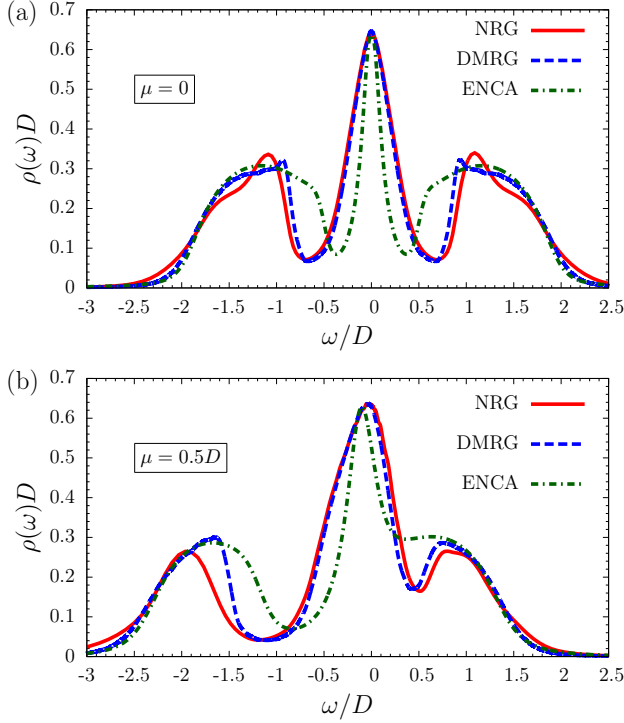


FIG. 4: (Color online) Spectral densities at $U = 2D$ and chemical potentials $\mu = 0$ (panel (a)) and $\mu = 0.5D$ (panel (b)). For NRG and DMRG $T = 0$ holds while for the ENCA $T = 0.027D \approx 0.15T^*$ ($\mu = 0$) and $T = 0.1D \approx 0.6T^*$ ($\mu = 0.5D$). For $\mu = 0.5D$, the fillings are $n_{\text{NRG}} \approx 0.580$, $n_{\text{DMRG}} \approx 0.592$, and $n_{\text{ENCA}} = 0.567$.

Fermi liquid scale T^* procured by the ENCA. This will be shown in the following.

For further analysis, we extract a common energy scale T^* from the data of all three methods. In microscopic Fermi liquid theory the low energy scale is proportional to the inverse mass enhancement⁸³ determined from the quasiparticle weight Z . The energy scale T_Z^* defined in this way reads

$$T_Z^* = ZD = \frac{1}{1 - \partial_\omega \text{Re}\Sigma(0)} D \quad (8)$$

and it is shown in Fig. 5 as function of the Coulomb repulsion U . For the two values of μ displayed in the figure, T_Z^* diminishes with increasing U and vanishes at the MIT. For larger values of the chemical potential, e.g., $|\frac{U}{2} \pm \mu| \gtrsim \frac{D}{2}$, the MIT will not occur anymore due to finite doping and T_Z^* will approach a constant value (not shown).

While the energy scale T_Z^* extracted from the two RG approaches agree quantitatively, the ENCA scale follows the same trend, but is lower by about a factor of two. This is in accord with results for the SIAM, i.e., without self-consistency, where the ENCA is known to produce the correct order of magnitude for the Kondo scale.^{20,52} The ENCA provides the exponential dependence of T_K on U , but the absolute values are slightly too low.⁴¹ Within

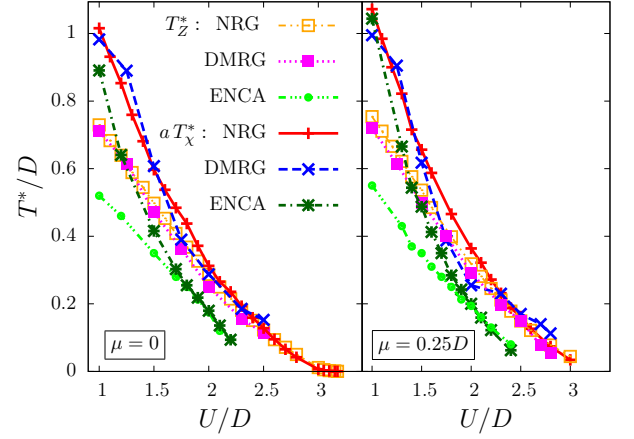


FIG. 5: (Color online) Fermi liquid scales T_Z^* and T_χ^* extracted from the quasiparticle weight and from the maximum of the spin susceptibility, respectively, as function of U for two values of the chemical potential. The magnetic scale T_χ^* is rescaled by a *single* factor $T_Z^* = aT_\chi^* = 3.125 \cdot T_\chi^*$ to obtain coinciding energies.

the self-consistency of the DMFT this tendency persists and it is slightly amplified.

Another estimate for the low energy scale can be defined from the characteristic excitation energies for spin fluctuations.⁸⁴ We determine a magnetic scale T_χ^* from the position of the maximum in the local dynamic magnetic susceptibility, $T_\chi^* = \omega_{\text{max}}$. This estimate is equivalent to the energy scale extracted from the linear slope in $\text{Im}\chi_{\text{mag}}(\omega)$ for small ω . As can be seen in Fig. 5, the two scales T_Z^* and T_χ^* of each method lie on top of each other at large U if T_χ^* is rescaled by a *single* factor a of order unity. Thus the low energy magnetic excitations and the single-particle excitations originate from the same physical process which is governed by a single energy scale. We will call such a behavior ‘universal’ in the context of the present work. For the SIAM such behavior is well known to occur in the Kondo regime. The DMFT self-consistency alters only quantitative aspects, but no qualitative ones. Hence Fig. 5 indicates universality in the metallic phase of the Hubbard model at large U where Kondo-correlated quasiparticles dominate the low energy physics.

We observe in Fig. 5 that the magnetic scale T_χ^* and the single-particle scale T_Z^* differ for small values of U (and at large doping, not shown) in analogy to what has been found in the SIAM.⁸⁵ T_Z^* and T_χ^* differ so that no universality can be established. A description of all excitations in terms of a *single* energy scale cannot be maintained. The Fermi liquid description is certainly still applicable, but all Landau parameters have to be determined independently.

Henceforth, we write $T^* = T_Z^*$ to represent the low energy scale and omit subscripts for simplicity.

The rescaled self-energy $T^*\Sigma(\omega)$, which determines the scattering rate of the Fermi liquid,⁸³ is plotted in Fig. 6

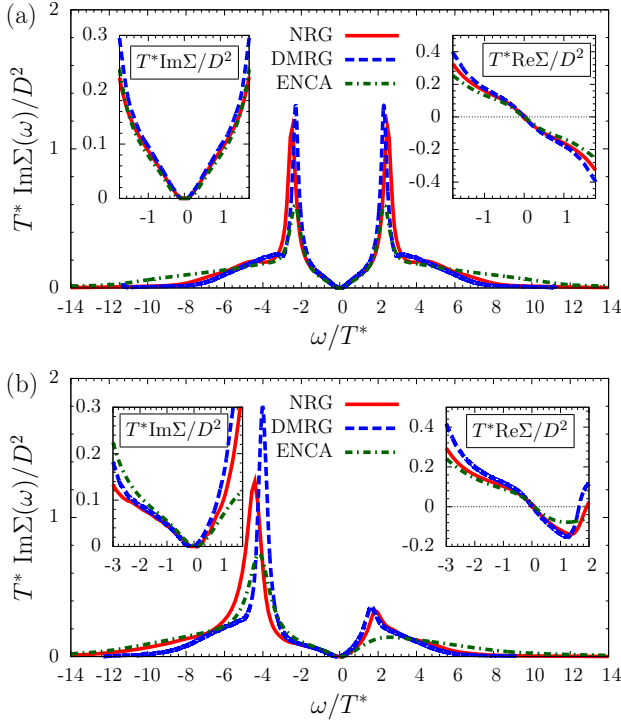


FIG. 6: (Color online) Rescaled self-energy $T^*\Sigma(\omega)$ for $U = 2D$ and (a) $\mu = 0$ (b) $\mu = 0.5D$ as a function of energy measured in units of the low energy scale T^* . Within the RG approaches we find $T^* \approx 0.31D$ and $T^* \approx 0.33D$ for $\mu = 0$ and $\mu = 0.5D$, respectively. In ENCA we find $T^* \approx 0.18D$ for $\mu = 0$ and $T^* \approx 0.2D$ for $\mu = 0.5D$, respectively. The temperatures are as in Fig. 4.

as function of ω/T^* for the same parameters as in Fig. 4. Generally, the agreement between the three methods is very good and deviations only occur at large energies, establishing the too low energy scale to be the main source of discrepancy between the ENCA and RG methods. The deviations for $\omega/T^* \gtrsim 1$ observable in panel (b) are on the one hand due to the improper description of correlated valence fluctuations^{17,52} and on the other hand due to the thermal broadening required in ENCA.

The rescaled dynamic magnetic susceptibility is depicted in Fig. 7 for two different chemical potentials. The peak positions from all three methods coincide but their heights differ. For the ENCA this is due to the finite temperature $T \propto \mathcal{O}(T^*)$ and the susceptibility is expected to increase if $T \rightarrow 0$. The use of raw NRG data without using the equation-of-motion trick⁶⁵ might be responsible for the discrepancies between the NRG and DMRG susceptibilities.

In the metallic regime, the universality conjectured before is supported by the fact that $T^*\text{Im}\chi_{\text{mag}}(\omega/T^*)$ approaches a universal function for large values of U in the half-filled case. This can be observed in Fig. 7b where the susceptibility from NRG is depicted for various values of U . For finite μ , however, $T^*\text{Im}\chi_{\text{mag}}(\omega/T^*)$ continues to grow with decreasing T^* indicating that valence fluc-

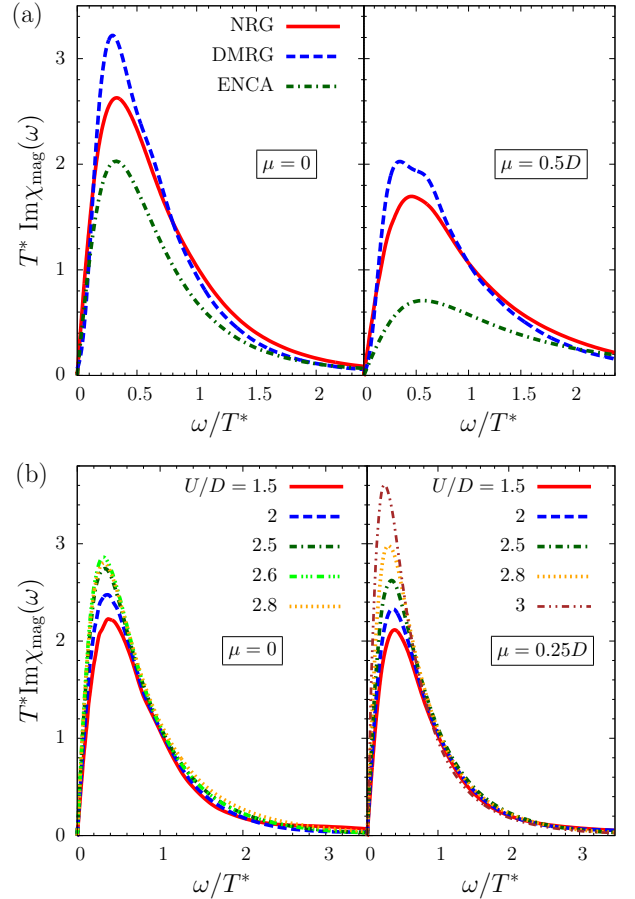


FIG. 7: (Color online) (a) Rescaled imaginary part of the magnetic susceptibility $T^*\text{Im}\chi(\omega/T^*)$ for $\mu = 0$ (left panel) and $\mu = 0.5D$ (right panel) at $U = 2D$ as a function of frequency. Parameters are as in Figs. 4. (b) $T^*\text{Im}\chi(\omega/T^*)$ vs. ω/T^* calculated with DMFT(NRG) for $\mu = 0$ (left panel) and $\mu = 0.25D$ (right panel) at various values of U .

tuations modify the low energy physics decisively, thus abolishing universality in the lattice model away from half-filling. This is in contrast to what is found in the impurity model.

The local charge susceptibility $\text{Im}\chi_{\text{charge}}(\omega)$ shown in Fig. 8 is strongly suppressed for small energies ω as consequence of the large Coulomb repulsion. This is particularly striking in comparison to the spin susceptibility. The characteristic energy scale of the charge susceptibility remains set by the interband excitation energy between the quasi-particle band and the Hubbard bands which is of the order $\sim \frac{U}{2} - |\mu|$.

In the curves obtained by the RG methods at half-filling, peaks emerge at the onset of the interband excitations as can be seen in Fig. 8 (left panel). They originate from the sharp features at the inner Hubbard band edges.¹⁵ As in the single particle spectrum, these are missing in the ENCA curve due to thermal broadening. Away from half-filling, the charge susceptibility increases due to the increased phase space at low en-

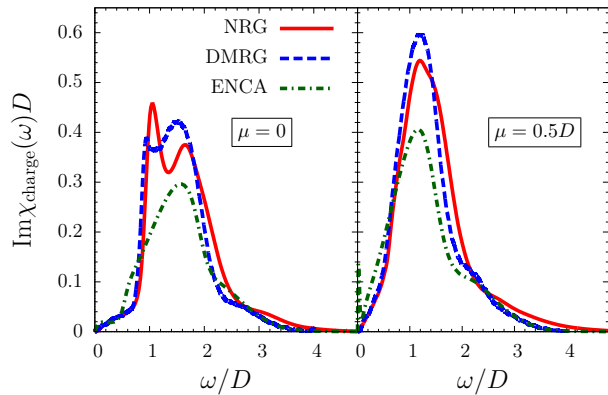


FIG. 8: (Color online) Imaginary part of the charge susceptibility for $\mu = 0$ (left panel) and $\mu = 0.5D$ (right panel) at $U = 2D$ as function of frequency in units of the half band-width D . Parameters are as in Fig. 4.

ergies. There, the ENCA reveals its limitations in the mixed-valence regime since at low temperature its threshold exponents generate an additional low frequency peak for $\omega \rightarrow 0$ which is expected to disappear if higher order vertex corrections were included.

For increasing Coulomb repulsion U , the spectral weight of $\text{Im}\chi_{\text{charge}}$ is shifted towards larger energies ω as illustrated in Fig. 2 in Ref. 15. In contrast, the position of the maximum of the spin susceptibility, which sets the scale T_{χ}^* , is shifted towards smaller energies with increasing U as shown in Fig. 7b. As a consequence, the energy scales of collective charge and spin excitations are clearly separated. This will turn out to be important for the observation of kinks.

Finally, we illustrate the full dependence of the spectral densities on the momentum via the bare dispersion ϵ_k according to

$$\rho(\omega, \epsilon_k) = \frac{1}{\pi} \text{Im} \frac{1}{\omega - i\delta - \epsilon_k - \Sigma(\omega)} \quad (9)$$

in the false-color plots in Fig. 9. The separation of single-particle energy scales and the influence of particle-hole asymmetry can be seen clearly. The almost flat ridge around $\omega = 0$ represents the narrow band of heavy quasiparticles which is well-separated in energy from the lower and upper Hubbard bands below and above $\omega = 0$. The coherence of the quasiparticle excitations is lost once ϵ_k reaches the scale T_{χ}^* where spin fluctuations become important. This causes a kink in $\text{Re}\Sigma$ as will be discussed in the following section. At large electron doping shown Fig. 9b, the upper Hubbard band and the quasiparticle band merge rendering charge and spin excitations equally important for positive energies. However, at negative energies, valence fluctuations are suppressed and the separation of energy scales persists.

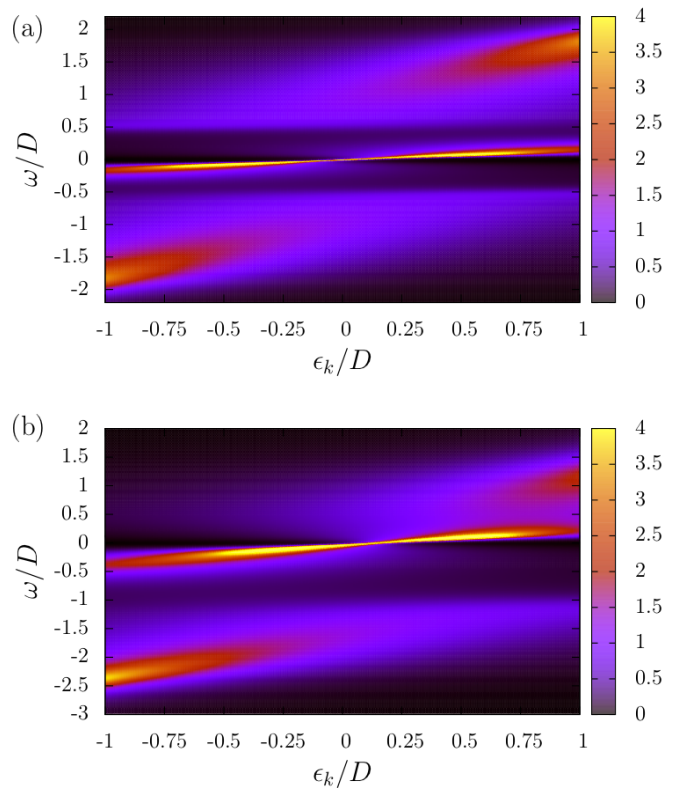


FIG. 9: (Color online) Spectral density $\rho(\omega, \epsilon_k)$ obtained within DMFT(ENCA) as function of frequency ω and bare electronic energy ϵ_k for $U = 2D$ at, (a) half-filling ($\mu = 0$) and (b) $\mu = 0.5D$.

IV. KINKS AND COLLECTIVE MODES

It is well known that the coupling of fermions to energetically low-lying bosonic modes causes kink-like structures in the fermionic dispersion. This picture is based on diagrammatic weak fermion-phonon coupling theory, see for instance Refs. 86 and 87, and references therein. The kink in the fermionic dispersion occurs roughly at the bare phonon energy. For stronger coupling, the diagrammatic approach breaks down^{88,89} and the kink feature persists but it does no longer occur at the bare phonon energy.⁹⁰ Roughly, the strength of the kink increases with the coupling between the fermionic and the bosonic modes.

Recently, it was demonstrated that kinks in the electronic dispersion are a generic feature of strongly correlated electron systems without any coupling to external bosons.⁵ Subsequently, it was shown that the kinks occurring in strongly interacting electron systems can be seen as result of the coupling of the fermions to the emergent collective excitations of magnetic character. Thus the system creates its own bosonic modes which in return generate the kinks.⁶

The original argument by Byczuk *et al.* for the kinks

was based on the three-peak structure in the spectral density $\rho(\omega)$, as shown in Fig. 4. Its essence is as follows: The many-body resonance extends around the Fermi level $\omega = 0$ from $\Omega_- < 0$ to $\Omega_+ > 0$, where Ω_{\pm} are the positions of the minima between the many-body resonance and the Hubbard bands.

Numerical results for the positions $|\Omega_{\pm}|$ of these minima calculated by NRG are shown in Fig. 10 as function of the quasiparticle weight Z . The lifting of the degeneracy of $|\Omega_{\pm}|$ upon doping is clearly visible. The NRG analysis suggests that the power law scaling $\Omega \propto Z^{1/4}$ holds for $Z \rightarrow 0$ (dashed line in Fig. 10 and in its inset).

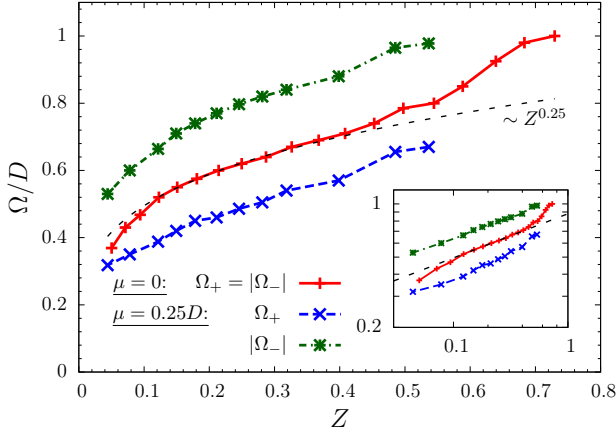


FIG. 10: (Color online) Positions of the minima between the many-body resonance and the Hubbard bands calculated by NRG as function of the quasiparticle weight Z . The inset shows the same data in a double-logarithmic plot. The dashed line depicts a power law $Z^{0.25}$ for comparison.

Furthermore, the KK relation implies that the real part of $G(\omega)$ is linear around $\omega = 0$ and that it has sharp maxima at positions r_{\pm} which are of the order of the half-width of the many-body resonance. In particular $|r_{\pm}| < |\Omega_{\pm}|$ holds. For the semi-elliptic DOS the self-consistency condition for the effective medium can be solved analytically by $\Gamma(z) = (D/2)^2 G(z)$. For general lattices, using this relation amounts up to approximating $\Gamma[G(z)]$ by the linear term of its moment expansion. Then Eq. (4) implies kinks in $\text{Re}\Sigma(\omega)$ at ω_{\star}^{\pm} with $|\omega_{\star}^{\pm}| < |\Omega_{\pm}|$.

An explicit expression for the position of the kinks can be obtained by describing the local Green function around the Fermi level by

$$G(\omega) \approx \frac{Z_{\text{loc}}}{\omega - \omega_0 - i(\gamma + \gamma'\omega)}. \quad (10)$$

The parameters ω_0 , γ , γ' , and Z_{loc} are determined from the physical quasiparticle weight Z and the non-interacting DOS alone. The kink positions ω_{\star}^{\pm} are calculated as the maxima of the second derivative of the

dressed dispersion

$$\omega_{\star}^{\pm} = \omega_0 \mp \frac{\gamma + \gamma'\omega_0}{\sqrt{1 + \gamma'^2}} \left(1 - \sqrt{2} \sqrt{1 \mp \frac{\gamma'}{\sqrt{1 + \gamma'^2}}} \right), \quad (11)$$

for details see supplement of Ref. 5, but note the differing sign of the inner square root. For the particle-hole symmetric case one has $\gamma' = \omega_0 = 0$ so that (11) reduces to $\omega_{\star}^{\pm} = \pm(\sqrt{2} - 1)\gamma$. For the semi-elliptic DOS $\gamma = ZD$ the kinks are thus located at $\omega_{\star}^{\pm} = \pm(\sqrt{2} - 1)ZD$.

Indeed, the kink positions in the numerical data for $\text{Re}\Sigma$ agree nicely with results obtained via Eq. (11). This is demonstrated for $\mu = 0.25D$ in Fig. 11 where the kink positions extracted for the DMRG and the NRG impurity solver are plotted as function of U/D . Only data for small doping and large repulsion is shown because for large doping and/or small repulsion the three-peak structure of $\rho(\omega)$ is not found so that the above analytical argument does not hold and the kinks cannot be resolved. For large doping and strong repulsion there still exists one kink in $\text{Re}\Sigma$ for which Eq. (11) still predicts the correct position (not shown).

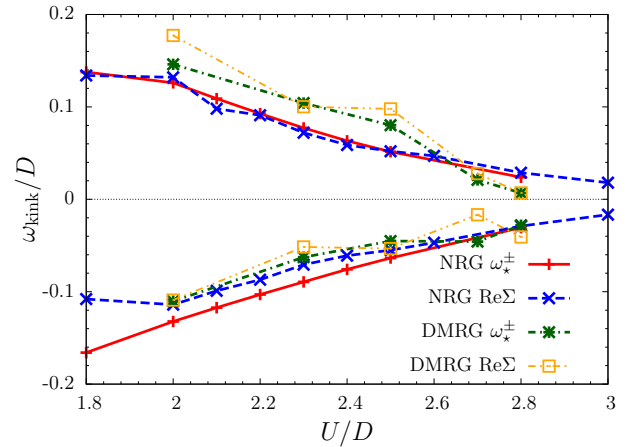


FIG. 11: (Color online) Comparison of the kink position from a numerical analysis of $\text{Re}\Sigma$ and from Eq. (11) for $\mu = 0.25D$ for the two RG impurity solvers as function of U .

The above analysis due to Byczuk et al. focusses on the mathematical structure of the equations defining the propagator and the self-energy. In Ref. 6 some of us showed for the half-filled case that the characteristic excitation energy of spin fluctuations agrees with the kink energy. Kinks in $\text{Re}\Sigma(\omega)$ lead via the KK relation to inflexion points in $\text{Im}\Sigma(\omega)$ at the same energies. This corresponds to a change in the quasiparticle lifetime $\tau \sim 1/\text{Im}\Sigma$. Inversely, this implies that humps in $\text{Im}\Sigma$ imply kinks in $\text{Re}\Sigma(\omega)$ via the KK transform. Hence, even though no explicit bosonic modes are included in the Hubbard model, the emergent collective spin excitations are responsible for the structures in $\text{Im}\Sigma(\omega)$ and thus for the kinks in $\text{Re}\Sigma$.

This argument is also applicable without particle-hole symmetry, i.e., for the doped model. The kinks

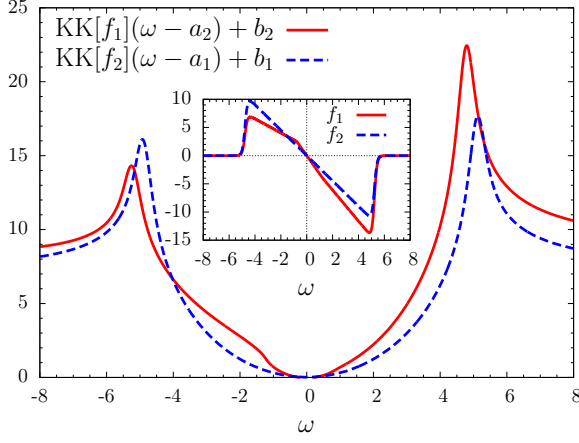


FIG. 12: (Color online) Illustration of the KK transforms of two test functions f_1 and f_2 , which are depicted in the inset. The first, f_1 displays a kink while the second (f_2) does not, but has the same average slope for small frequencies. The KK transforms are shifted by a_i, b_i such that $\text{KK}[f_i](-a_i) + b_i = 0$.

in $\text{Re}\Sigma(\omega)$ are still associated with additional inflexion points in $\text{Im}\Sigma(\omega)$ which are related to changes in the relaxation mechanism. To illustrate this view qualitatively, we mimic a kink in $\text{Re}\Sigma(\omega)$ by the function f_1 depicted in Fig. 12 and include for comparison f_2 without a kink. Then we study the differences in the KK transforms which correspond to the imaginary part. While $\text{KK}[f_2]$ is governed by a wide parabola in the range $\omega \in (-4, 4)$, $\text{KK}[f_1]$ displays a noticeable hump starting below the frequency of the kink. A parabolic fit would hold only in the interval $\omega \in (-1, 1)$.

DMFT self-energies computed with the NRG are shown in Fig. 13a. The dashed lines in the upper panel indicate the linear fits to $\text{Re}\Sigma(\omega)$ used to determine the kink positions. Fig. 13a displays the same qualitative features as Fig. 12 though they are less pronounced. The physical model does not display mathematically sharp kinks as the test function f_1 does. The real part $\text{Re}\Sigma(\omega)$ in Fig. 13a displays two kinks. The one at negative frequencies is fairly clear, the one at positive frequencies is fairly weak. Correspondingly, the humps in $\text{Im}\Sigma(\omega)$ are clearly visible at negative frequencies, but only weakly discernible at positive frequencies. The kinks, which mark the beginning of the humps, indeed occur at about $T_\chi = \frac{1}{3}T^*$ ($\equiv \frac{1}{3}T_Z^*$), cf. Fig. 5, in agreement with the previous finding at half-filling.⁶

A parabolic description in terms of the Fermi liquid scale $(\omega/T^*)^2$ is possible, but only up to about $|\omega/T^*| \approx 0.3$, again in accord with the finding at half-filling.⁶ The scattering rate as given by $\text{Im}\Sigma(\omega)$ decreases compared to a pure $(\omega/T^*)^2$ behavior with increasing $|\omega|$.

This picture is consistent with the renormalization group flow and the RG fixed points of the effective site for a converged metallic DMFT solution. For $T^* \gg |\omega| \rightarrow 0$, the physics is determined by a line of strong coupling

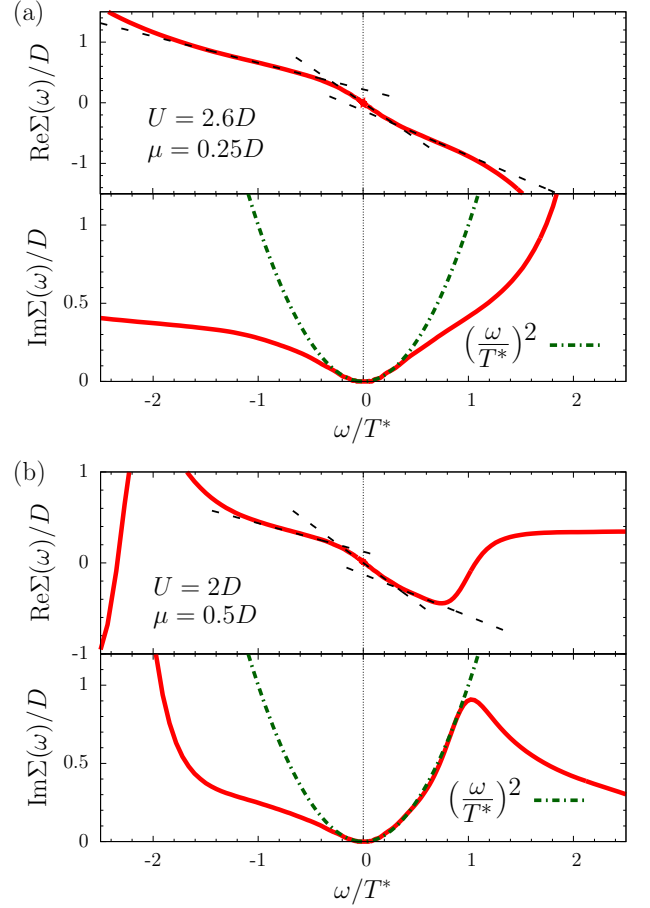


FIG. 13: (Color online) (a) $\text{Re}\Sigma(\omega)$ (upper panel) and $\text{Im}\Sigma(\omega)$ (lower panel) at finite doping as function of ω/T^* obtained from DMFT(NRG). The dashed lines in the upper panel indicate linear fits used to determine kink positions. In the lower panel the parabola $(\omega/T^*)^2$ expected from Fermi liquid theory is included for comparison. The coherence scale $T^* \approx 0.16D$ is the low-energy scale for $U = 2.6D$, cf. Fig. 5. (b) Same as in panel (a), but for $\mu = 0.5D$ at $U = 2D$. Note that the kink at positive frequencies is very weak and concomitantly $\text{Im}\Sigma(\omega)$ displays parabolic behavior up to $\omega \approx T^*$ except for a very shallow hump.

(SC) fixed points which describes a Fermi-liquid with broken particle-hole symmetry.^{19,59} Its characteristic energy scale is given by T^* , and $\text{Im}\Sigma(\omega) \propto (\omega/T^*)^2$. With increasing frequency, however, the system is described by the unstable local-moment (LM) fixed point. The dynamic Kondo singlet is broken on a scale $T_K \propto T_\chi^*$ by singlet-triplet excitations and the quasiparticles disintegrate at higher excitation energies, leaving a free local spin coupled to the conduction band. As a consequence, the scattering is reduced and the self-energy is increasing much slower than close to the SC fixed point. Spin-flip scattering dominates the self-energy in the vicinity of the LM fixed point.

Therefore, the single-particle self-energy retraces the crossover from the LM to the SC fixed point. At very

high frequencies the magnetic scattering is weak, and the physics of the Hubbard model is determined by the local charging energies derived from the atomic picture. Hence the self-energies depicted in Fig. 6 are low and featureless at very high frequencies. At intermediate frequencies, the spin-flip scattering provides an additional decay channel on top of a weakly correlated, particle-hole asymmetry conduction band. This additional decay channel reveals itself in $\text{Im}\Sigma(\omega)$ as the humps at intermediate energies, cf. Figs. 12 and 13. At low energy scales, the spin-flip scattering is replaced in $\text{Im}\Sigma(\omega)$ by the Fermi-liquid parabola determined by T^* for $|\omega| \rightarrow 0$.

At larger electron doping, only the lower Hubbard band is well separated from the quasiparticle band, see Fig. 4. The particle-hole asymmetry and the correlated valence fluctuations matter for positive excitation energies. The scales for spin and charge excitations are not well separated so that both channels contribute to the self-energy. The $\text{Im}\Sigma(\omega)$ remains almost quadratic in ω for $\omega > 0$ even on the scale of $\omega \approx T^*$ as can be seen in Fig. 13b for $\mu = 0.5D$ at $U = 2D$. Only a minute hump occurs in the quasiparticle decay rate at the spin excitation energy and consequently only a very weak kink occurs at positive energies. Even though the spin-susceptibility shows a pronounced maximum, the accessibility of low-energy charge fluctuations for positive energies suppresses the kink, in accord with the two conditions stated in the Introduction.

At negative excitation energies, correlated low-energy valence fluctuations cannot be excited so that the charge energy scale is well separated from the coherence scale T^* . Thus the kink and the corresponding hump are distinct at negative frequencies.

The above discussion shows that kinks can be directly linked to physical processes in the system. As in the symmetric case, the kink positions in the self-energy correlate with the positions of the maxima of the spin susceptibility, i.e., T_χ^* , which is shown in Fig. 14 for two values of μ . The values for both quantities from all three methods coincide and the small deviations can be understood from the strengths and the weaknesses of the methods as discussed in Sect. III A. The kink positions ω_* equal T_χ^* for $T_\chi^* \rightarrow 0$. This clearly supports the view that the spin fluctuations are responsible for the kinks. Deviations occur for larger energies corresponding to smaller values of U . There, the Fermi liquid description in terms of a single energy scale does not apply anymore since T_χ^* and T_Z^* stem from combinations of different types of excitations, and non-universal valence fluctuations play a role. Additionally, kinks are less pronounced for small U and hence their positions are harder to determine unambiguously. For smaller U the spin fluctuations do not yet behave like emergent collective bosonic modes, and the charge and spin excitations are not well separated in energy.

Finally, we study the doping dependence of the kinks at fixed interaction. Generic results are depicted in Fig. 15 for hole doping. As observed in Fig. 14 the kink positions and energy scale of the spin fluctuations coincide

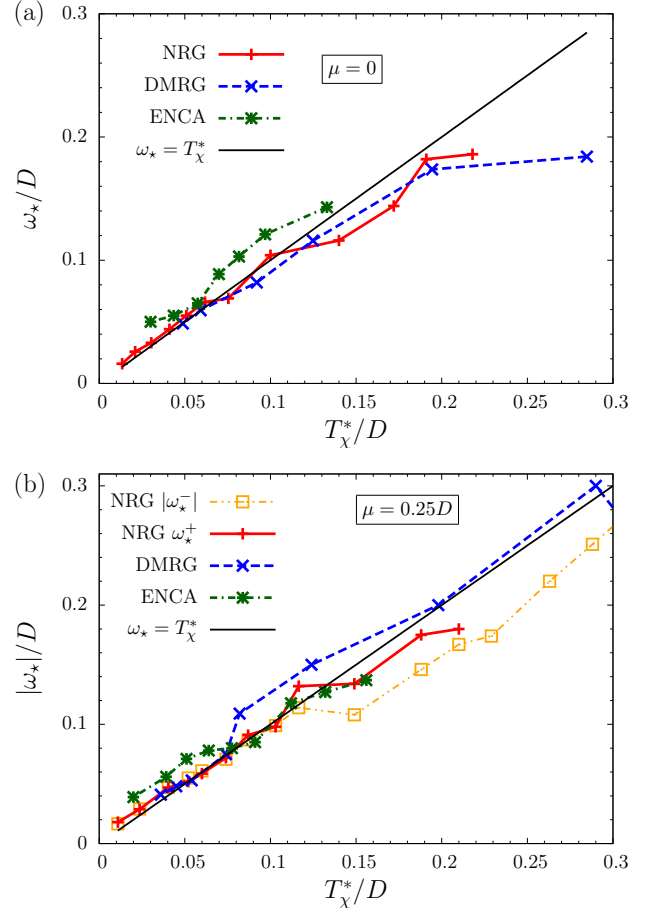


FIG. 14: (Color online) Kink energies ω_\star^\pm as function of the frequency of the maximum T_χ^*/D in the imaginary part of the spin susceptibility for (a) $\mu = 0$ and (b) $\mu = 0.25D$.

$\omega_\star^+ \approx |\omega_\star^-| \approx T_\chi^*$ for small doping $\delta \lesssim 0.07$. For larger doping the particle-hole asymmetry implies that ω_\star^+ and $|\omega_\star^-|$ differ from each other and hence from T_χ^* . For hole doping, we find $\omega_\star^+ > T_\chi^* > |\omega_\star^-|$ but the deviations are rather small. Up to an offset, all three energy scales depend essentially linearly on doping. The energy scales rise upon increasing doping. The two panels of Fig. 15 compare the doping dependence of the kinks for two different values of U . Clearly, a larger value of U decreases the energy scale of the kinks as one would expect for a magnetic energy scale.

At this point, a comparison to experiment is in order. The experimentally best studied strongly correlated systems displaying kinks are the superconducting cuprates. It is presently still debated whether these kinks are of phononic^{91,92} or of magnetic origin.^{9,93} Our calculation based on DMFT and a semi-elliptic DOS is too far away from the experimental situation to make a quantitative comparison. But it is interesting to note that the kink positions observed at low temperatures in underdoped high T_c materials indeed display a linear behavior with offset very similar to the one in Fig. 15. Even the num-

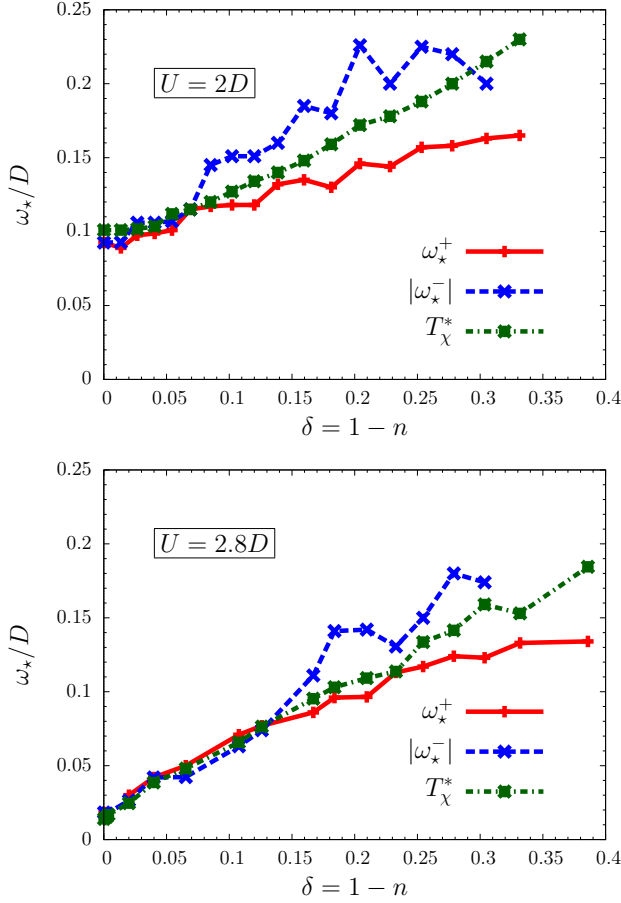


FIG. 15: (Color online) Dependence of the kink positions ω_{\star}^{\pm} and of the scale of the magnetic modes on hole doping for $U = 2D$ (upper panel) and for $U = 2.8D$ (lower panel) obtained from DMFT(NRG).

bers are in the experimental range^{7,8} of about 30 meV at zero doping to 120 meV at $\delta = 0.15$ if we assume $D = 1.4\text{eV}$ and $U = 4\text{eV} \approx 2.8D$. The latter number is too high by a factor 2 compared to the cuprates,⁸ but this is not astounding in view of the approximation made in the present study.

We emphasize that we consider only the low-energy kinks. These can be expected to be described with an effective low-energy single-band Hubbard model which is based on the existence of the Zhang-Rice singlets.⁹⁴ Any statements on the formation of Zhang-Rice singlets and on dispersion features at higher energies such as “waterfalls” which require a multiband description, see for instance Ref. 95, are beyond the scope of the present work. Still, the doping dependence observed here is in accord with a magnetic explanation of the kinks in the cuprates.

V. SUMMARY

In this paper, we have focussed on the physical origin of kinks in the electronic dispersion of strongly correlated electronic systems *without* coupling to external bosons. Exemplarily, we have studied the doped Hubbard model in dynamic mean-field theory at zero temperature.

Three different numerical algorithms have been employed for solving the self-consistent impurity problem for the dynamic mean-field theory and their results have been compared. We have found a very good agreement between all three impurity solvers. This is quite remarkable considering their very different nature and corroborates the validity of our evaluations. We distinguish the two numerical renormalization group approaches (NRG and DMRG) which can be applied directly at zero temperature and the analytical ENCA which is based on the summation of a large subset of diagrams of an expansion in the hybridization.

The NRG is an efficient numerical approach for arbitrary temperatures and very precise at small frequencies, but washes out spectral details at higher frequencies due to the logarithmic discretization and the concomitant broadening. The DMRG is the most resource consuming approach because it requires a separate run for each spectral frequency. It is used here as a zero temperature method, though extensions to finite temperatures are in principle possible. To access exponentially small frequencies a logarithmic discretization would be necessary.⁹⁶ For equidistant discretization, however, the DMRG exhibits a very good resolution at all frequencies. The ENCA is fastest in the computation and provides data with arbitrary resolution at all frequencies. But it suffers from Fermi liquid pathologies below the coherence temperature T^* which prevent its reliable application at very small temperatures.

With all these three different methods, we have studied the kinks in the dispersion of the interacting electron system away from half-filling. We have established that the appearance of the kink is linked to dominant spin fluctuations at low energies. In particular, the position of the kinks in energy is intimately linked to the spin-fluctuation scale T_{χ}^* where the magnetic susceptibility exhibits its maximum. Additionally, the occurrence of kinks requires a substantial energy separation between the charge fluctuation scale $U/2 - |\mu|$ and T_{χ}^* , i.e. $U/2 - |\mu| \gg T_{\chi}^*$. This is clearly the case in the strongly correlated regime at large values of $U \gtrsim 2D = W$ where W is the bandwidth. Therefore, the low-lying bosonic modes of the electronic system modify the electronic dispersion on the scale T_{χ}^* at sufficiently strong electron-electron interaction U .

Universality, i.e., the possibility to describe the low-energy dynamics in units of a single energy scale, is only observed close to half-filling where the scale is set by the spin-fluctuation scale T_{χ}^* . For large doping and/or weaker interaction, there is no clear separation between the spin- and charge-fluctuation scale and universality is

lost.

Finally, we have compared the doping dependence of the kinks in the single-band Hubbard model with kinks measured with angle-resolved photoemission in planar cuprates. In spite of the much higher complexity of the cuprates compared to our model study, the energy scales are qualitatively reproduced: Magnetically induced kinks evolve from 30 meV to about 120 meV with increasing hole doping for $U = 1.4W$.

In conclusion, we extended the view that emergent modes of the electronic system can generate kinks in the electronic dispersion in analogy to materials with strong electron-phonon coupling even away from half-filling, provided (i) that there is a significant energy separation between the high and low energy scale, $T_\chi^*/D \ll 1$ and which implies that we are in the strong coupling regime $U/W \gtrsim 1$, and (ii) that the charge energy scale is

much larger than T_χ^* . Note that in the studied strongly correlated system the ratio T_χ^*/D takes the role of the ratio of the Debye frequency over the Fermi energy in coupled electron-phonon systems. We expect that this a generic feature and very similar results will apply in many other related systems with clearly separated energy scales and strong emergent modes.

Acknowledgments

We acknowledge financial support from the Deutsche Forschungsgemeinschaft under AN 275/6-2 and super-computer support by the NIC, FZ Jülich under project No. HHB00. One of us (PG) was supported by a PhD grant of the Studienstiftung des deutschen Volkes.

-
- * E-Mail:sebastian.schmitt@tu-dortmund.de
- ¹ N. Ashcroft and J. Wilkins, Phys. Lett. **14**, 285 (1965).
 - ² G. Mahan, *Many-Particle Physics* (Plenum Press, New York, 1981).
 - ³ T. Pruschke, M. Jarrell, and J. Freericks, Adv. Phys. **44**, 187 (1995).
 - ⁴ A. Georges, G. Kotliar, W. Krauth, and M. J. Rozenberg, Rev. Mod. Phys. **68**, 13 (1996).
 - ⁵ K. Byczuk, M. Kollar, K. Held, Y.-F. Yang, I. A. Nekrasov, T. Pruschke, and D. Vollhardt, Nat. Phys. **3**, 168 (2007).
 - ⁶ C. Raas, P. Grete, and G. S. Uhrig, Phys. Rev. Lett. **102**, 076406 (2009).
 - ⁷ A. A. Kordyuk, S. V. Borisenko, A. Koitzsch, J. Fink, M. Knupfer, B. Büchner, H. Berger, G. Margaritondo, C. T. Lin, B. Keimer, et al., Phys. Rev. Lett. **92**, 257006 (2004).
 - ⁸ A. A. Kordyuk, S. V. Borisenko, V. B. Zabolotnyy, J. Geck, M. Knupfer, J. Fink, B. Büchner, C. T. Lin, B. Keimer, H. Berger, et al., Phys. Rev. Lett. **97**, 017002 (2006).
 - ⁹ T. Dahm, V. Hinkov, S. V. Borisenko, A. A. Kordyuk, V. B. Zabolotnyy, J. Fink, B. Büchner, D. J. Scalapino, W. Hanke, and B. Keimer, Nat. Phys. **5**, 217 (2009).
 - ¹⁰ A. Hofmann, X. Y. Cui, J. Schäfer, S. Meyer, P. Höpfner, C. Blumenstein, M. Paul, L. Patthey, E. Rotenberg, J. Bünenmann, et al., Phys. Rev. Lett. **102**, 187204 (2009).
 - ¹¹ E. Müller-Hartmann, **74**, 507 (1989).
 - ¹² P. G. J. van Dongen, F. Gebhard, and D. Vollhardt, **76**, 199 (1989).
 - ¹³ G. S. Uhrig and R. Vlaming, Phys. Rev. Lett. **71**, 271 (1993).
 - ¹⁴ G. S. Uhrig and R. Vlaming, Ann. Phys. (Leipzig) **507** or **4**, 778 (1995).
 - ¹⁵ C. Raas and G. S. Uhrig, Phys. Rev. B **79**, 115136 (2009).
 - ¹⁶ M. Jarrell, Phys. Rev. Lett. **69**, 168 (1992).
 - ¹⁷ S. Schmitt, *Excitations, Two-Particle Correlations and Ordering Phenomena in Strongly Correlated Electron Systems from a Local Point of View*, (PhD thesis, available at <http://tuprints.ulb.tu-darmstadt.de/1264/>, TU Darmstadt 2008).
 - ¹⁸ U. Schollwöck, Rev. Mod. Phys. **77**, 259 (2005).
 - ¹⁹ R. Bulla, T. Costi, and T. Pruschke, Rev. Mod. Phys. **80**, 395 (2008).
 - ²⁰ T. Pruschke and N. Grewe, Z. Phys. B **74** (1989).
 - ²¹ H. Keiter and Q. Qin, Physica B **163**, 594 (1990).
 - ²² P. Nozières, *Theory of Interacting Fermi Systems* (Addison-Wesley, Reading, Massachusetts, 1997).
 - ²³ N. Grewe and F. Steglich, *Handbook on the Physics and Chemistry of Rare Earths* (North-Holland, 1991), vol. 14, p. 343.
 - ²⁴ P. Coleman, *Handbook of Magnetism and Advanced Magnetic Materials* (J. Wiley and Sons, 2007), vol. 1: Fundamentals and Theory., pp. 95–148.
 - ²⁵ E. H. Lieb and F. Y. Wu, Phys. Rev. Lett. **20**, 1445 (1968).
 - ²⁶ E. H. Lieb and F. Y. Wu, Physica A **321**, 1 (2003).
 - ²⁷ F. Essler, H. Frahm, F. Göhmann, A. Klümper, and V. Korepin, *The One-Dimensional Hubbard Model* (Cambridge University Press, Cambridge, United Kingdom, 2005).
 - ²⁸ A. Georges, in *Lectures on the physics of highly correlated electron systems VIII*, edited by A. Avella and F. Mancini (2004), vol. 715 of *AIP Conf. Proc.*, pp. 3–74.
 - ²⁹ J. Kunes, I. Leonov, M. Kollar, K. Byczuk, V. I. Anisimov, and D. Vollhardt, Eur. Phys. J. Special Topics **180**, 5 (2010).
 - ³⁰ W. Metzner and D. Vollhardt, Phys. Rev. Lett. **62**, 324 (1989).
 - ³¹ E. Müller-Hartmann, Z. Phys. B **74**, 507 (1989).
 - ³² A. Georges and G. Kotliar, Phys. Rev. B **45**, 6479 (1992).
 - ³³ H. Kajueter and G. Kotliar, Phys. Rev. Lett. **77**, 131 (1996).
 - ³⁴ B. Radzimirski and R. J. Wojciechowski, Acta Physica Polonica A **111**, 753 (2007).
 - ³⁵ M. Caffarel and W. Krauth, Phys. Rev. Lett. **72**, 1545 (1994).
 - ³⁶ Q. Si, M. J. Rozenberg, G. Kotliar, and A. E. Ruckenstein, Phys. Rev. Lett. **72**, 2761 (1994).
 - ³⁷ M. Feldbacher and F. F. Assaad, Phys. Rev. B **63**, 073105 (2001).
 - ³⁸ A. N. Rubtsov, V. V. Savkin, and A. I. Lichtenstein, Phys. Rev. B **72**, 035122 (2005).
 - ³⁹ P. Werner, A. Comanac, L. de' Medici, M. Troyer, and A. J. Millis, Phys. Rev. Lett. **97**, 076405 (2006).
 - ⁴⁰ E. Gull, A. J. Millis, A. I. Lichtenstein, A. N. Rubtsov,

- M. Troyer, and P. Werner, Rev. Mod. Phys. **83**, 349 (2011).
- ⁴¹ N. Grewe, S. Schmitt, T. Jabbens, and F. B. Anders, J. Phys.: Condens. Matter **20**, 365217 (2008).
- ⁴² J. Holm and K. Schönhammer, Solid State Commun. **69**, 969 (1989).
- ⁴³ K. Haule, C.-H. Yee, and K. Kim, Phys. Rev. B **81**, 195107 (2010).
- ⁴⁴ G. Baym and L. P. Kadanoff, Phys. Rev. **124**, 287 (1961).
- ⁴⁵ G. Baym, Phys. Rev. **127**, 1391 (1962).
- ⁴⁶ H. Keiter and J. C. Kimball, J. Appl. Phys. **42**, 1460 (1971).
- ⁴⁷ H. Keiter and J. C. Kimball, Int. J. Magn. **1**, 233 (1971).
- ⁴⁸ N. Grewe and H. Keiter, Phys. Rev. B **24**, 4420 (1981).
- ⁴⁹ H. Keiter and G. Morandi, Phys. Rep. **109**, 227 (1984).
- ⁵⁰ N. Grewe, Z. Phys. B **53**, 271 (1983).
- ⁵¹ Y. Kuramoto, Z. Phys. B **53**, 37 (1983).
- ⁵² S. Schmitt, T. Jabbens, and N. Grewe, Phys. Rev. B **80**, 235130 (2009).
- ⁵³ Y. Kuramoto and E. Müller-Hartmann, J. Magn. Magn. Mater. **52**, 122 (1985).
- ⁵⁴ N. E. Bickers, Rev. Mod. Phys. **59**, 845 (1987).
- ⁵⁵ M. Jarrell and T. Pruschke, Phys. Rev. B **49**, 1458 (1994).
- ⁵⁶ T. A. Costi, J. Kroha, and P. Wölfle, Phys. Rev. B **53**, 1850 (1996).
- ⁵⁷ K. G. Wilson, Rev. Mod. Phys. **47**, 773 (1975).
- ⁵⁸ H. R. Krishna-murthy, J. W. Wilkins, and K. G. Wilson, Phys. Rev. B **21**, 1003 (1980).
- ⁵⁹ H. R. Krishna-murthy, J. W. Wilkins, and K. G. Wilson, Phys. Rev. B **21**, 1044 (1980).
- ⁶⁰ F. B. Anders and A. Schiller, Phys. Rev. Lett. **95**, 196801 (2005).
- ⁶¹ F. B. Anders and A. Schiller, Phys. Rev. B **74**, 245113 (2006).
- ⁶² R. Peters, T. Pruschke, and F. B. Anders, Phys. Rev. B **74**, 245114 (2006).
- ⁶³ A. Weichselbaum and J. von Delft, Phys. Rev. Lett. **99**, 076402 (2007).
- ⁶⁴ M. Yoshida, M. A. Whitaker, and L. N. Oliveira, Phys. Rev. B **41**, 9403 (1990).
- ⁶⁵ R. Bulla, A. C. Hewson, and T. Pruschke, J. Phys.: Condens. Matter **10**, 8365 (1998).
- ⁶⁶ R. Bulla, T. A. Costi, and D. Vollhardt, Phys. Rev. B **64**, 045103 (2001).
- ⁶⁷ F. B. Anders, Phys. Rev. B **71**, 121101 (2005).
- ⁶⁸ S. R. White, Phys. Rev. Lett. **69**, 2863 (1992).
- ⁶⁹ S. R. White, Phys. Rev. B **48**, 10345 (1993).
- ⁷⁰ U. Schollwoeck, Ann. of Phys. **326**, 96 (2011).
- ⁷¹ D. J. García, K. Hallberg, and M. J. Rozenberg, Phys. Rev. Lett. **93**, 246403 (2004).
- ⁷² S. Ramasesha, S. K. Pati, H. R. Krishnamurthy, Z. Shuai, and J. L. Bredas, Synthetic Metals **85**, 1019 (1997).
- ⁷³ T. D. Kühner and S. R. White, Phys. Rev. B **60**, 335 (1999).
- ⁷⁴ E. Jeckelmann, Phys. Rev. B **66**, 045114 (2002).
- ⁷⁵ D. J. García, E. Miranda, K. Hallberg, and M. J. Rozenberg, Physica B **398**, 407 (2007).
- ⁷⁶ D. J. García, E. Miranda, K. Hallberg, and M. J. Rozenberg, Phys. Rev. B **75**, 121102(R) (2007).
- ⁷⁷ E. Miranda, D. J. García, K. Hallberg, and M. J. Rozenberg, Physica B **403**, 1465 (2008).
- ⁷⁸ C. Raas, *Dynamic Density-Matrix Renormalization for the Symmetric Single Impurity Anderson Model* (PhD thesis, available at <http://www.raas.de>, Universität Köln, 2005).
- ⁷⁹ C. Raas and G. Uhrig, Eur. Phys. J. B **45**, 293 (2005).
- ⁸⁰ M. Karski, C. Raas, and G. S. Uhrig, Phys. Rev. B **72**, 113110 (2005).
- ⁸¹ M. Karski, C. Raas, and G. S. Uhrig, Phys. Rev. B **77**, 075116 (2008).
- ⁸² T. Pruschke, D. L. Cox, and M. Jarrell, Europhys. Lett **21**, 593 (1993).
- ⁸³ C. Varma, Z. Nussinov, and W. van Saarloos, Phys. Rep. **361**, 267 (2002).
- ⁸⁴ M. Jarrell, J. E. Gubernatis, and R. N. Silver, Phys. Rev. B **44**, 5347 (1991).
- ⁸⁵ S. Schmitt and F. B. Anders, Phys. Rev. B **81**, 165106 (2010).
- ⁸⁶ S. Engelsberg and J. R. Schrieffer, Phys. Rev. **131**, 993 (1963).
- ⁸⁷ D. J. Scalapino, in *Superconductivity*, edited by R. D. Parks (Marcel Dekker, New York, 1969), p. 449.
- ⁸⁸ P. Benedetti and R. Zeyher, Phys. Rev. B **58**, 14320 (1998).
- ⁸⁹ D. Meyer, A. C. Hewson, and R. Bulla, Phys. Rev. Lett. **89**, 196401 (2002).
- ⁹⁰ J. Bauer and G. Sangiovanni, Phys. Rev. B **82**, 184535 (2010).
- ⁹¹ A. Lanzara, P. V. Bogdanov, X. J. Zhou, S. A. Kellar, D. L. Feng, E. D. Lu, T. Yoshida, H. Eisaki, A. Fujimori, K. Kishio, et al., Nature **412**, 510 (2001).
- ⁹² A. S. Mishchenko, Phys. Usp. **52**, 1193 (2009).
- ⁹³ M. Eschrig, Ann. Phys. (NY) **55**, 47 (2006).
- ⁹⁴ F. C. Zhang and T. M. Rice, Phys. Rev. B **37**, 3759 (1988).
- ⁹⁵ D. S. Inosov, J. Fink, A. A. Kordyuk, S. V. Borisenko, V. B. Zabolotnyy, R. Schuster, M. Knupfer, B. Büchner, R. Follath, H. A. Dürr, et al., Phys. Rev. Lett. **99**, 237002 (2007).
- ⁹⁶ S. Nishimoto and E. Jeckelmann, J. Phys. Cond. Mat. **16**, 613 (2004).